

**Wavefront engineering with optimally loaded absorbing metamirrors**Athanasios N. Papadimopoulos *Department of Electrical and Computer Engineering, Aristotle University of Thessaloniki, Thessaloniki GR-54124, Greece*Alisher Duspayev *Department of Physics, University of Michigan, Ann Arbor, Michigan 48109, USA*Nikolaos L. Tsitsas *Department of Informatics, Aristotle University of Thessaloniki, Thessaloniki GR-54124, Greece*Nikolaos V. Kantartzis *Department of Electrical and Computer Engineering, Aristotle University of Thessaloniki, Thessaloniki GR-54124, Greece*Constantinos Valagiannopoulos \**Department of Physics, Nazarbayev University, Nur-Sultan KZ-010000, Kazakhstan*

(Received 8 June 2020; revised 11 March 2021; accepted 12 April 2021; published 27 April 2021)

Modifying the wavefront of electromagnetic fields is one of the most significant operations in a variety of photonic components from spatial wave modulators and optical deflectors to focusing lenses and reflectarray nanoantennas. Metamirrors comprising dielectric and plasmonic layers back-to-back are found to serve well such a purpose of wavefront transformation for reflected waves with use of tiny scatterers placed at positions of enhanced field and by exploiting the absorbing mechanism of these bilayers. Even though the efficiency of the configurations is not high due to the presence of losses, the tailoring of the reflective wave pattern is successful given the simplicity of the considered setups. In particular, numerous optimal designs that anomalously reflect the incoming plane waves or convert them into cylindrical ones have been determined by trying and testing every combination from a large set of available media. Thus, extra degrees of freedom are provided in modeling such modules that are vital for several wavefront engineering applications.

DOI: [10.1103/PhysRevB.103.165307](https://doi.org/10.1103/PhysRevB.103.165307)**I. INTRODUCTION**

Controlling the amplitude and phase of electromagnetic waves as they propagate in space is a generic and critical function behind a myriad of microwave and photonic devices. Such a process has become easier and more feasible with the advent of metasurfaces, where subwavelength nanoparticles modify locally the reflection and transmission coefficients from a flat boundary and “rewrite” at will the laws of diffraction [1]. The planarly distributed inclusions that create this effective boundary condition vary from elliptical dielectric nanoposts, offering complete control of refractive polarization [2], to resonant nanocubes accomplishing extreme light bending and focusing [3,4] and printed patches on unit cells for arbitrary tailoring of transmissive wavefronts [5]. Similar wavefront engineering aims are greatly served by the development of general synthesis formulations that provide the correct susceptibility tensors for the desired transformation [6] and give rise to intelligent metasurfaces with continuously tunable surface features for multiple reconfigurable operations [7,8]. Nonlinear elements have been, also, employed to

further enhance the local power concentration and refractive resolution [9] or achieve asymmetric light transport allowing for the implementation of one-way photonic devices such as unrivaled optical valves and diodes [10].

In most of the aforementioned approaches, the control of the wavefront concerns the transmissive signal; however, the fabrication of free-standing ultrathin structures is not always convenient. Indeed, the surface is commonly patterned on an impenetrable base helping the integration into larger optical systems and securing low interference with neighboring components. Therefore, the old concept of millimeter-wave reflectarrays [11] has been carried over to optical wavelengths making ultraefficient metamirrors achieving total control of reflectivity flow [12]. Explicitly, retroreflecting utilities are identified via cascaded metasurfaces [13], while arrays of small bianisotropic inclusions can fully reflect electromagnetic waves with any desired phase distribution [14]. Metamirrors can also comprise electronically tunable meta-atoms with voltage-controlled varactor diodes for wavefront control [15] in microwave antenna setups [16] and anisotropic cells for broadband achromatic polarization engineering [17].

In this work, we examine the possibility of reflective wavefront manipulation through optimized bilayers that are found to absorb very effectively the visible light regardless of the

\*konstantinos.valagiannopoulos@nu.edu.kz

incidence angle [18]. Such setups are composed of a lossless dielectric layer backed by a thin metallic strip; the wave phase changes as it travels into the first piece and matches with the second one where the absorption occurs. This absorbing mechanism creates a large signal enhancement at specific positions inside the dielectric slab and, if additional appliances are placed at them, a metasurface admitting the engineering of reflections is formed. A long list of insulating and plasmonic media is considered and for every single combination of them the design is optimized for dimensions, making it suitable to work as an efficient metamirror. Such an exhaustive, trial-and-error approach is routinely employed for a variety of different layouts from layered crystals [19] and core-shell nanoparticles [20] to semiconducting heterojunctions [21] and radiating wires [22].

Two cases of wavefront engineering are examined, the first of which is a transformer of the incoming planar wavefront into a curved one by means of a single rod located at the maximum signal position. Since the bilayer effectively absorbs all the incoming rays, the reflection will be mainly created by the optically small cylinder and will have almost circular isophase contours, regardless of the incidence angle; in other words, any plane wave input is converted into a small-signal “dimplelike” reflection. This utility can be crucial in setups requiring optical focus without holographic operation [23] but, most importantly, in devices calling for sharp frequency sensing [24] or beam forming [25]. The second investigated case concerns the effect of anomalous reflection achieved via a periodic pattern of multiple pins along the line of enhanced field. This channeling of the incoming power along several directions permits the device to be operated as a photonic multipoint network of controllable scattering matrix [26] or used in retroreflectors [27] and wave steering setups [28]. In addition, similar structures have been extensively used for switching the absorbed power [29], achieving spatial mode multiplexing [30] and creating directive radiation in visible-light communications [31]. Hence we provide multiple optimal metamirrors performing wavefront manipulations, vital in several photonic engineering applications.

## II. MOTIVATION AND STRATEGY

A planar bilayer configuration, as depicted in Fig. 1, is the minimal Cartesian structure supporting resonances which, in turn, lead to various optimal operations. A characteristic case of highly performing thin bilayers concerns wide-angle absorption of visible light (at free-space wavelength  $\lambda_0$ ) and has been recently elaborated [18]. In this context, the incoming illumination first meets a dielectric slab (of relative permittivity  $\varepsilon_1$ ) which corrects its phase to get properly matched with the second metallic slab (of relative permittivity  $\varepsilon_2$ ). At the optimally absorbing regime, the reflections are negligible, while the field decays and gets absorbed into the plasmonic layer, yielding negligible transmission. On the contrary, the signal oscillates into the intermediate dielectric layer with period equal to the local wave number  $\lambda_1 = \lambda_0/\sqrt{\text{Re}[\varepsilon_1]}$ , giving enhanced values at specific points for most of the incidence angles  $\theta$ . An illustration of the spatial distribution of the field is given in Fig. 1, where the used Cartesian coordinate system ( $x, y, z$ ) is defined as well as the thickness of the dielectric

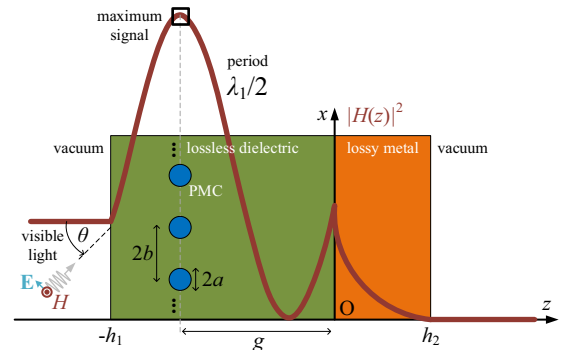


FIG. 1. Sketch of the considered setup. A bilayer comprising a lossless dielectric and a metallic substrate exhibits signal enhancement somewhere into the first region. We examine the case of one or infinite magnetically conducting (PMC) cylinders positioned at the maximization position while the structure is obliquely excited by plane wave of visible light.

$h_1$ , the size of the metallic slab  $h_2$ , and the position of the maximal signal  $z = -g$ . Note that due to the permittivity discontinuity ( $\text{Re}[\varepsilon_1]\text{Re}[\varepsilon_2] < 0$ ) at  $z = 0$ , while both materials are magnetically inert, such a field enhancement occurs only when the magnetic field  $\mathbf{H}$  is parallel to the  $y$  axis.

Given their small optical thickness, the regarded structures (invariant along the  $y$  axis) can certainly operate as planar metasurfaces able to strongly interact with the excitation, if properly loaded along the maximum signal plane  $z = -g$ . To serve this aim, we consider, again, most of the designs of our related prequel work [18] and find the positions  $g$  at which the field  $|\mathbf{H}|^2 = |H\hat{y}|^2 = |H|^2$  is maximized. The obtained results are presented in Table I, where the oscillation frequency  $f$ , the geometrical characteristics ( $h_1, h_2$ ), and the maximal signal locations  $g$  are shown for each combination of dielectrics (rows) and metals (columns). The color of each box indicates the visible light illumination, while a blank gray box corresponds to poor performance. Following the well-described optimization process [18], but solely for the  $\mathbf{H}\parallel\hat{y}$  polarization, we conclude to bilayers that exhibit tiny wide-angle reflections, averaged by the  $\mathcal{J}\{\star\} = \int_0^{\pi/2} \star \cos \theta d\theta$  operator (which considers only the energy exchange along the normal-to-interfaces  $z$  axis) combined with a large field enhancement  $|H(z = -g)|^2$ .

By inspection of Table I, one directly infers that all the colors of the visible spectrum are well represented, whereas the preference of certain materials for specific frequencies  $f$  may be, also, recorded. In particular, the bilayers using germanium are working only under red color illumination, where  $\text{Re}[\varepsilon_1]$  takes substantial values, while GaP-based designs absorb blue and violet light. On the other hand, other materials like GaAs or crystalline silicon operate optimally at different wavelengths in proportion to what is the metallic surface on which they are grown. Our key objective is to utilize the wide-angle absorbing bilayers of Table I, combined with simple nanostructures located at maximal signal position  $z = -g$ , to manipulate the overall reflection.

It should be stressed that there is a price to be paid for using as base design a maximally absorbing structure and that is nothing more than the high losses yielding a weak reflectivity

TABLE I. Frequencies (indicated also by the corresponding color of the visible spectrum), optimal material thicknesses ( $h_1$ ,  $h_2$ ), and position ( $g$ ) of the scatterers for each combination of the available materials for the proposed setup of Fig. 1. Every bilayer design is correlated with different optimal thickness selection of the two layers and rod locations, while blank (shaded) boxes correspond to poor reflecting performance.

	Aluminum (Al)	Copper (Cu)	Gold (Au)	Platinum (Pt)	Silver (Ag)	Titanium (Ti)
<b>Aluminium Antimonide (AlSb)</b>	560 THz $h_1 = 82$ nm $h_2 = 31$ nm $g = 51$ nm	550 THz $h_1 = 76$ nm $h_2 = 77$ nm $g = 43$ nm	560 THz $h_1 = 72$ nm $h_2 = 91$ nm $g = 41$ nm	520 THz $h_1 = 89$ nm $h_2 = 60$ nm $g = 54$ nm	570 THz $h_1 = 72$ nm $h_2 = 67$ nm $g = 42$ nm	500 THz $h_1 = 93$ nm $h_2 = 76$ nm $g = 55$ nm
<b>Gallium Arsenide (GaAs)</b>	510 THz $h_1 = 101$ nm $h_2 = 28$ nm $g = 63$ nm	520 THz $h_1 = 88$ nm $h_2 = 75$ nm $g = 51$ nm	530 THz $h_1 = 84$ nm $h_2 = 84$ nm $g = 48$ nm	400 THz $h_1 = 136$ nm $h_2 = 52$ nm $g = 84$ nm	540 THz $h_1 = 84$ nm $h_2 = 65$ nm $g = 50$ nm	
<b>Gallium Phosphide (GaP)</b>	750 THz $h_1 = 61$ nm $h_2 = 34$ nm $g = 37$ nm	680 THz $h_1 = 67$ nm $h_2 = 67$ nm $g = 39$ nm	660 THz $h_1 = 68$ nm $h_2 = 91$ nm $g = 39$ nm	670 THz $h_1 = 72$ nm $h_2 = 52$ nm $g = 43$ nm	780 THz $h_1 = 50$ nm $h_2 = 89$ nm $g = 27$ nm	630 THz $h_1 = 78$ nm $h_2 = 71$ nm $g = 46$ nm
<b>Germanium (Ge)</b>		400 THz $h_1 = 98$ nm $h_2 = 75$ nm $g = 58$ nm	400 THz $h_1 = 97$ nm $h_2 = 70$ nm $g = 57$ nm		400 THz $h_1 = 98$ nm $h_2 = 75$ nm $g = 58$ nm	
<b>Indium Phosphide (InP)</b>	400 THz $h_1 = 153$ nm $h_2 = 25$ nm $g = 97$ nm	490 THz $h_1 = 109$ nm $h_2 = 101$ nm $g = 64$ nm	490 THz $h_1 = 97$ nm $h_2 = 70$ nm $g = 57$ nm		430 THz $h_1 = 131$ nm $h_2 = 59$ nm $g = 79$ nm	
<b>Silicon (Si)</b>	730 THz $h_1 = 48$ nm $h_2 = 43$ nm $g = 29$ nm	640 THz $h_1 = 61$ nm $h_2 = 75$ nm $g = 35$ nm	640 THz $h_1 = 59$ nm $h_2 = 92$ nm $g = 33$ nm	580 THz $h_1 = 77$ nm $h_2 = 54$ nm $g = 46$ nm	740 THz $h_1 = 42$ nm $h_2 = 94$ nm $g = 23$ nm	570 THz $h_1 = 76$ nm $h_2 = 77$ nm $g = 44$ nm

compared to the power of the incoming waves. However, this fact is not expected to lead in extremely low efficiencies that will render the proposed designs useless, since we are planning to place the extra equipment exactly at the location of maximized field. Furthermore, selecting these highly absorbing bilayers to load, offers the advantage of increased electromagnetic compatibility and low interference because the structure is built on an impenetrable metallic film; that would not be the case if a transmissive metasurface was used instead. Importantly, if one employs a perfect reflector to back the device without the absorption operation of our bilayers, the primary reflection from this will be much stronger than the scattering from the nanoparticles which will practically nullify the efficiency of the design. Finally, our structure is quite simple and uses scatterers located into a lossless dielectric host instead of being free-standing, which will be more challenging from the construction point of view. In this sense, we propose a number of different metamirrors performing disruptive wavefront transformations with elementary setups.

Regarding the actual fabrication of the proposed setups, it is certainly not easy or straightforward; however, there are available methods that can be followed. In particular, with colloidal lithography fabrication [32] an array of spheres is deposited on a penetrable base and the reactive ion etching follows [33]. In this way, nanocylinders can be carved and the empty space between them is filled with the lossless dielectric of our choice. Apart from top-down lithographic techniques, a plethora of bottom-up fabrication methodologies can be

implemented as well. For example, vapor-liquid-solid (VLS) method is quite commonly used [34]; more specifically, the nanowires are chemically grown from a substrate material with the help of catalyst droplets which are subsequently removed [35].

### III. SINGLE ROD TRANSFORMER

#### A. Mathematical formulation

Perhaps the simplest possible structural perturbation of the obtained wide-angle absorbing designs is to place a small two-dimensional (2D) obstacle at the maximal signal positions, indicated by Table I. Since these devices operate when the magnetic field is parallel to  $y$  axis, one can consider a perfectly magnetically conducting (PMC) cylindrical rod of radius  $a$  located along  $(z, x) = (-g, 0)$  axis. These PMC rods have the property of nullifying the magnetic field across their volume to keep the magnetic flux density finite since the magnetic permeability is giant; that feature renders them strong scatterers. The background field  $H_{\text{back}}(z, x)$  excites the induced surface magnetic current  $M$  flowing along  $y$  axis at the rod (measured in V/m) which, in turn, produces scattered field  $H_{\text{scat}}(z, x)$ . In this context, the total magnetic field in all the considered regions is written as a sum of the background (in the absence of the scatterer) and the scattered field:  $H(z, x) = H_{\text{back}}(z, x) + H_{\text{scat}}(z, x)$ . It is well known that, for suppressed time dependence  $e^{+i2\pi ft}$ , the scattering term is

given by the so-called scattering integral [36]:

$$H_{\text{scat}}(z, x) = -i \frac{k_0}{\eta_0} \int_{(C)} M(l) G(z, x, Z, X) dl, \quad (1)$$

where  $(C)$  is the circumference of the PMC obstacle,  $k_0 = 2\pi f/c = 2\pi/\lambda_0$  the wave number,  $c$  the speed of light, and  $\eta_0$  the wave impedance, all into vacuum. Note that the magnitude of background field  $|H_{\text{back}}|^2$  is independent from  $x$ . The magnetic currents are actually materialized via electric currents of different direction; however, in this study we employ the modified Maxwell laws and the corresponding boundary conditions that incorporate magnetic current excitation [37].

The usage of PMC properties for the scatterers may sound somehow uncommon; however, it is extensively used for modeling purposes in order to fit better with the considered polarization of waves. By utilizing such a mathematical model, the formulated boundary value problem becomes much easier to solve and thus one can demonstrate in a more direct way the proposed operational regime with use of analytical tools. In particular, we expect that the drawn conclusions are not substantially affected by the texture of the nanorods as long as they can work as strong scatterers. But, on the other hand, PMC are just materials with vanishing magnetic fields into their volume, as indicated above; such a property can be mimicked well by media with large magnetic permeabilities. For example, ferromagnetic shells with huge permeability have been fabricated to play the role of cloaks for magnetostatic fields [38], while nanotubes with similar characteristics have been deposited to serve switching operations [39]. Finally, the permeability of materials can be substantially enhanced by controlling their inherent defects in their crystalline structure [40], while even the concept of perfect magnetic wall has been experimentally achieved in planar geometries as an outcome of plasmonic resonances [41].

The notation  $G(z, x, Z, X)$  in (1) is used for the scalar Green's function of the bilayer, providing the field at the observation point  $(z, x)$  when a 2D line source is placed along the axis  $(Z, X)$ . Particularly, Green's function,  $G$ , comprises a singular (primary) term,  $G_{\text{prim}}$ , corresponding to the response of the source if it radiates in an unbounded medium and a smooth (secondary) one,  $G_{\text{sec}}$ , expressing the effect of the additional structural formations [42]. If the source  $(Z, X)$  is posed into the semiconducting layer  $-h_1 < Z < 0$ , the primary component of Green's function is written as  $G_{\text{prim}} = -\frac{i}{4} H_0^{(2)}(k_1 \sqrt{(z-Z)^2 + (x-X)^2})$ , where  $k_1 = k_0 \sqrt{\varepsilon_1}$  and  $H_v^{(2)}$  is the  $v$ th order of second-type Hankel function. Concerning the secondary component, it takes the form

$$G_{\text{sec}}(z, x, Z, X) = \int_{-\infty}^{+\infty} d\beta e^{-i\beta(x-X)} \times \begin{cases} R(\beta, Z) e^{\kappa_0 z}, & z < -h_1 \\ A(\beta, Z) e^{-\kappa_1 z} + B(\beta, Z) e^{\kappa_1 z}, & -h_1 < z < 0 \end{cases}, \quad (2)$$

where the  $\beta$ -dependent radiation functions  $\kappa_0, \kappa_1$  are evaluated with positive real parts:  $\kappa_0 = \kappa_0(\beta) = \sqrt{\beta^2 - k_0^2}$  and  $\kappa_1 = \kappa_1(\beta) = \sqrt{\beta^2 - k_1^2}$ . The explicit forms of quantities  $R(\beta, Z)$ ,  $A(\beta, Z)$ ,  $B(\beta, Z)$ , as well as the background mag-

netic field  $H_{\text{back}}(z, x)$  everywhere in the considered area ( $z \in \mathbb{R}$ ) under an oblique incidence excitation  $H_{\text{inc}}(z, x) = e^{-ik_0(z \cos \theta + x \sin \theta)}$ , are not shown for brevity.

Under the assumption that the optical size of the rod is very small ( $k_0 a \ll 1$ ), it is sensible to assume that the magnetic current is invariant around the rod  $M(l) \cong M$  and, most importantly, impose the boundary condition for null magnetic field only at the center of the cylinder:  $H_{\text{scat}}(-g, 0) = -H_{\text{back}}(-g, 0)$ . By adopting this thin-wire approximation [42] and conducting the integration [43] of the singular Green's component in (1), one can obtain  $M$  along the PMC pin as follows:

$$M = \frac{H_{\text{back}}(-g, 0)}{i \frac{k_0}{\eta_0} (2\pi a) \left[ -\frac{i}{4} H_0^{(2)}(k_1 a) + G_{\text{sec}}(-g, 0, -g, 0) \right]}. \quad (3)$$

Once  $M$  is computed, the scattered magnetic field  $H_{\text{scat}}(z, x)$  into free space ( $z < -h_1$ ) is directly evaluated via (1). Through stationary phase approximation, the scattered power in the far region ( $z \rightarrow -\infty$ ) behaves as [44]

$$p_{\text{scat}}(r, \varphi) \sim \frac{(k_0 a)^2}{k_0 r} |M|^2 |R(-k_0 \sin \varphi, -g)|^2 \cos^2 \varphi, \quad (4)$$

where  $(r, \varphi, z)$  is the equivalent cylindrical coordinate system centralized at the axis of the PMC rod ( $z = -h_1 - r \cos \varphi$  and  $x = -r \sin \varphi$ ).

## B. Numerical results

Based on the above aspects, the  $H_{\text{scat}}$  field for  $z < -h_1$ , added to the reflected plane wave  $H_{\text{ref}}$  (with a spatial dependence  $e^{-ik_0(-z \cos \theta + x \sin \theta)}$ ) of the rod-free structure, constitutes the overall reaction of our metasurface. Given the fact that most of the designs of Table I give negligible reflections, the field distribution  $H_{\text{scat}}$  in the vicinity of air/dielectric interface  $z = -h_1$  defines the transformed wavefront of the metamirror when it is excited by a plane wave. Observe that, due to its small size of the rod, its response will be of moderate magnitude and thus it is meaningful to be compared with the reflection amplitude. If the ratio  $|H_{\text{scat}}|^2/|H_{\text{ref}}|^2$  is large, the single rod can transform the incoming planar wavefront to almost a cylindrical one, owing to its tiny cross section ( $k_0 a \ll 1$ ). Evidently, such a conversion does not concern the far region  $z \rightarrow -\infty$ , where the reflected power will always be nonzero (no matter how small the reflective coefficient is) contrary to  $p_{\text{scat}}$ , which vanishes (no matter how powerful the magnetic current  $M$  is), according to (4). Therefore, the proposed setups can act as wavefront transformers in the near region only.

In this framework and by selecting the AlSb-Au bilayer at  $f = 560$  THz from Table I, Fig. 2(a) illustrates the ratio of the  $|H_{\text{scat}}(z, x)|^2$  amplitude over the incident one  $|H_{\text{inc}}|^2$  with respect to  $x$ , for various distances  $z$  into vacuum. Despite the fact that the considered bilayers exhibit very high absorption, the scattered power by an extremely small ( $a = 1$  nm) cylinder cannot be deemed negligible, compared to the incident field, at least in the vicinity of the air/dielectric interface  $z = -h_1$ . Furthermore, as  $z$  increases, the field distribution diminishes and gradually flattens, as smaller and smaller parts of the scattered wavefront are depicted. For the sake of comparison, Fig. 2(a) shows the  $|H_{\text{ref}}|^2/|H_{\text{inc}}|^2$  ratio, as well, which indi-

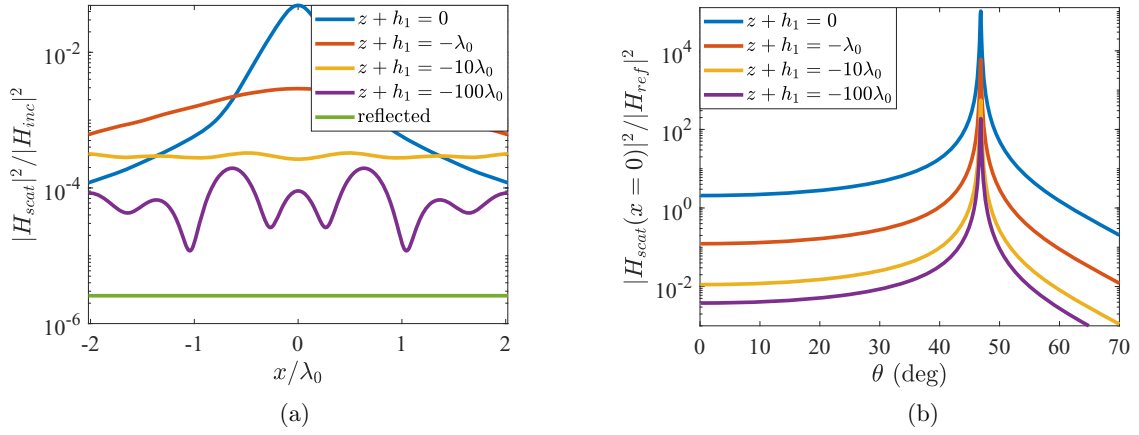


FIG. 2. Scattered field produced by an  $a = 1$  nm PMC rod and normalized by (a) the incident one,  $|H_{\text{scat}}|^2 / |H_{\text{inc}}|^2$ , as a function of  $x/\lambda_0$  (for an optimal  $\theta \cong 47^\circ$ ) and (b) the reflected one,  $|H_{\text{scat}}|^2 / |H_{\text{ref}}|^2$ , as a function of the incidence angle,  $\theta$ , across different constant- $z$  planes, parallel to the air/dielectric interface (for  $x = 0$ ). All results correspond to the AlSb-Au bilayer of Table I.

icates that, even at a  $100\lambda_0$  distance, the scattered component is much larger than the reflected one.

The preceding phenomenon is more clearly demonstrated in Fig. 2(b), where the maximum (at  $x = 0$ ) ratio  $|H_{\text{scat}}|^2 / |H_{\text{ref}}|^2$  is plotted as a function of the incidence angle  $\theta$  for the same design and constant- $z$  planes of Fig. 2(a). It becomes apparent that the transformation is far more efficient at a specific  $\theta$  range around an optimal one [herein,  $\theta \cong 47^\circ$ , which is also the case in Fig. 2(a)]; nonetheless, the presented ratio has nonzero values for the considered distances or incident directions. Given the inherent trade-off between maximum  $|H_{\text{scat}}|^2 / |H_{\text{ref}}|^2$  and the wide-angle character of a configuration, the specific setup leans on the former design requirement, while other designs from Table I may exhibit considerably higher angular insensitivity but smaller peaks in similar scenarios. In other words, all the metamirrors, featured in Table I, are suitable to operate as near-field transformers at diverse angular ranges.

In Fig. 3(a), we show three characteristic designs with different sharpness with respect to  $\theta$ , optimally operated at different visible frequencies (indicated by the color of the curve) and various incidence angles. One may directly discern that AlSb-Pt pair exhibits substantial wide-angle behavior since the power ratio does not fall below 10 for an angular extent up to  $40^\circ$ . On the contrary, the Si-Au pair gives

significant angular selectivity and lower reflections (high  $|H_{\text{scat}}|^2 / |H_{\text{ref}}|^2$ ). Furthermore, in all the considered cases, the values of the represented quantity close to normal incidence are almost invariant since our wide-angle designs are optimized according to a metric emphasizing the contribution from  $\theta = 0^\circ$ . Nevertheless, the power ratios decrease rapidly for grazing angles, as the reflection increases significantly. To substantiate these observations, Figs. 3(b) and 3(c) display the frequency dependence of the  $|H_{\text{scat}}(z, x = 0)|^2 / |H_{\text{ref}}|^2$  enhancement ratio for certain designs from Table I, around the operational frequency  $f$ . From the sharp variations, it can be deduced that the proposed structures are suitable for sensing and filtering applications, which opt for highly selective frequency responses.

Probing further, the requisite of negligible transmission through optical components is proven to be vital in chip design, when low crosstalk levels and compact device packaging are required; that is a key motive for investigating a reflecting metasurface (metamirror) in this study. However, the same goal of transforming the incident plane wave into a cylindrical reflecting waveform can be served by a number of alternative setups that enable the incoming field to fully transmit. Therefore, it is meaningful to compare the scattered power ratio of the featured designs with the corresponding ones from existing setups, emphasizing that the zero trans-

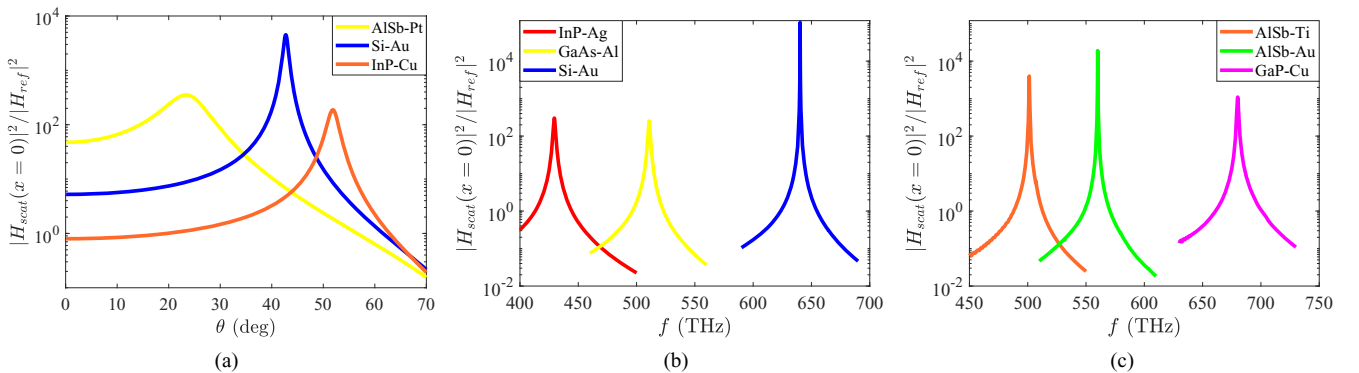


FIG. 3. Maximum  $|H_{\text{scat}}(z, x = 0)|^2 / |H_{\text{ref}}|^2$  as a function of the (a) incidence angle,  $\theta$  (for the central frequency) and (b), (c) operational frequency,  $f$  (for the optimal angles) for selected designs of Table I. The scattering is caused by a PMC rod of radius  $a = 1$  nm.

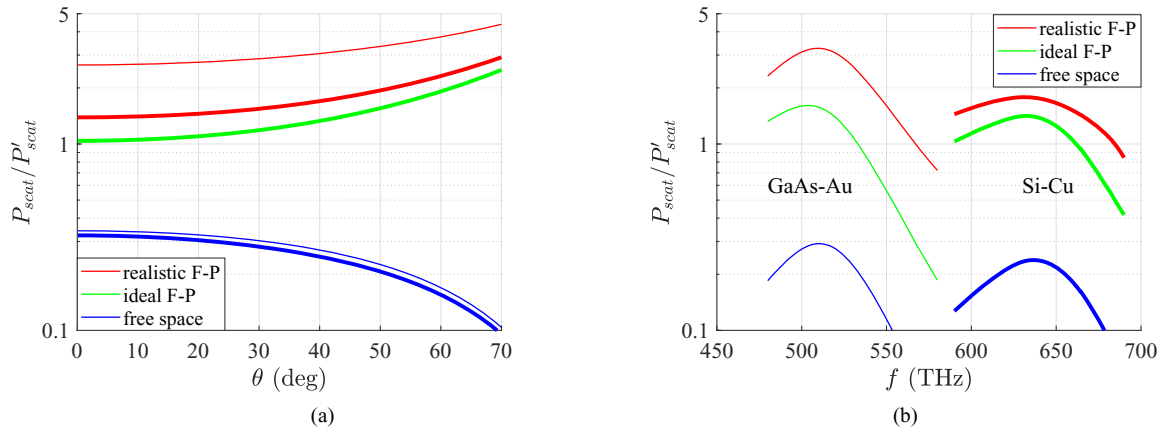


FIG. 4. Ratio  $P_{\text{scat}}/P'_{\text{scat}}$  of the power scattered by a PMC rod of radius  $a = 1$  nm, when using the proposed bilayers,  $P_{\text{scat}}$ , and three setups [i.e., a lossy (realistic) F-P resonator, a lossless (ideal) F-P resonator, and a single rod standing in free space],  $P'_{\text{scat}}$ , as a function of the (a) incidence angle  $\theta$  and (b) central operational frequency  $f$ . Thin lines correspond to a GaAs-Au bilayer at  $f = 520$  THz and thick lines refer to a Si-Cu bilayer at  $f = 640$  THz.

mission constraint is not satisfied by the latter ones. To this objective, Fig. 4(a) presents the  $P_{\text{scat}}/P'_{\text{scat}}$  ratio of the power scattered by the same rod as a function of the incidence angle, for two of the proposed designs (GaAs-Au and Si-Cu),  $P_{\text{scat}}$ , and three alternative setups,  $P'_{\text{scat}}$ . Specifically for the latter, we consider a Fabry-Pérot resonator comprising the lossless version of the same semiconductor used in our bilayers, both optimally matched for the same angle. Furthermore, we examine the same resonator in the presence of the actual losses and finally the rod free-standing into the vacuum background. By inspection of Fig. 4(a), it is clear that the represented  $P_{\text{scat}}/P'_{\text{scat}}$  ratio does not possess negligible values for any angle of incidence; consequently, the scattering power from our device is comparable to other similar ones serving alternative purposes. On the other hand, in Fig. 4(b), we depict the same scattered-power ratio for the aforementioned arrangements as a function of the central operational frequency  $f$ . Again, the ratio receives nonzero values over the entire spectrum, which are close to unity (or even larger) in the vicinity of  $f$ .

Our analysis focuses, also, on the critical issue of wide-angle wavefront manipulation, namely the transformation of arbitrarily incident plane waves to cylindrical ones. Hence it is desirable that the proposed structures reflect in a similar way the incident illumination regardless of its initial direction. In Fig. 5, this feasibility is demonstrated by picking one of the reported designs (AlSb-Pt at  $f = 520$  THz) and exciting it at different angles ( $\theta = 0^\circ, 10^\circ, 20^\circ, 30^\circ$ ). The overall response field  $\text{Re}[H_{\text{scat}} + H_{\text{ref}}]$ , which is the sum of the background reflection  $\text{Re}[H_{\text{ref}}]$  and the cylinder's scattering  $\text{Re}[H_{\text{scat}}]$ , is normalized by the (unitary) magnitude of the incident field  $|H_{\text{inc}}|$  and represented with the same color scale. As observed, in all cases, the magnetic field distribution resembles strongly a cylindrical wavefront, regardless of the incidence direction, especially for angles close to the bilayer's optimal ones ( $\theta = 23^\circ$ ).

### C. PEC rod treatment

In the aforementioned formulation, the cylinder that loads the bilayer structure is considered to be PMC which facil-

itates the extraction of a straightforward solution, owing to the polarization ( $\mathbf{H} \parallel \hat{\mathbf{y}}$ ) and the 2D nature of the configuration (dependent only on  $x$  and  $z$ ). However, similar results are obtained when the rod is deemed perfectly electrically conducting (PEC), with the difference that the dominant angular momentum orders  $e^{i\nu\varphi}$  will not be the omnidirectional ( $\nu = 0$ ) but the dipolar ones ( $\nu = \pm 1$ ). In the following, we briefly describe the basic steps that permit solution to the corresponding PEC-loaded bilayer, just to address the related boundary value problem.

If the rod placed into the lossless dielectric requires a vanishing electric field around its surface and its interior, the analysis can be modified accordingly. In particular, let

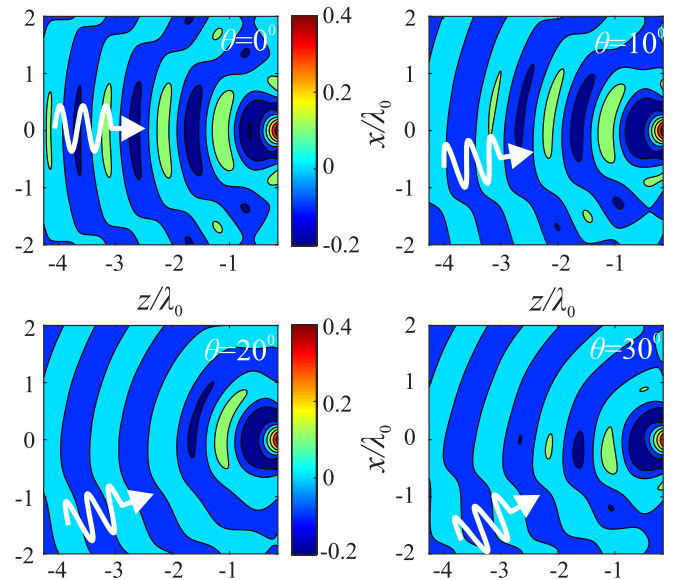


FIG. 5. Spatial distribution of the normalized magnetic field response  $\text{Re}[H_{\text{ref}} + H_{\text{scat}}]/|H_{\text{inc}}|$  of the wavefront transformer on  $xz$  plane for various angles of incidence  $\theta$  (these specific distributions correspond to AlSb-Pt design of Table I working at  $f = 520$  THz). White arrows denote the direction of incident wave and scattering is developed by a PMC rod of radius  $a = 5$  nm.

us assume that the azimuthal surface current  $K(\varphi)$  can be approximated by its omnidirectional and bipolar Fourier terms since the size of the cylinder is optically small ( $k_0a \ll 1$ ):

$$K(\varphi) \cong K_0 + K_{+1}e^{+i\varphi} + K_{-1}e^{-i\varphi}. \quad (5)$$

Express the Green's function  $G$  in the polar coordinate system centralized at the cylindrical rod, namely the observation point is denoted by  $(r, \varphi)$  while the source point by  $(\rho, \phi)$ , and the scattered magnetic field  $H_{\text{scat}}$  takes the form of [45]:

$$H_{\text{scat}}(r, \varphi) = a \int_0^{2\pi} K(\phi) \frac{\partial G(r, \varphi, \rho, \phi)}{\partial \rho} \Big|_{\rho=a} d\phi. \quad (6)$$

Accordingly, the surface current can be determined from (6) by applying the boundary condition for vanishing tangential ( $\varphi$ -directed) electric field around the cylinder  $r = a$ , namely

$$\int_0^{2\pi} K(\phi) F(\varphi, \phi) d\phi = -\frac{1}{a} \frac{H_{\text{back}}(r, \varphi)}{\partial r} \Big|_{r=a} \equiv W(\varphi), \quad (7)$$

where  $F(\varphi, \phi) \equiv \frac{\partial^2 G(r, \varphi, \rho, \phi)}{\partial r \partial \rho} \Big|_{r=\rho=a}$  and  $H_{\text{back}}$  is the background (parallel to  $y$  axis) magnetic field in the absence of the cylinder expressed in the local coordinate system  $(r, \varphi)$ . Furthermore,  $F$  can be accurately approximated by the first two azimuthal orders; in particular,  $F(\varphi, \phi) \cong F_0(\phi) + F_{+1}(\phi)e^{+i\varphi} + F_{-1}(\phi)e^{-i\varphi}$ . Similarly,  $W(\varphi) \cong W_0 + W_{+1}e^{+i\varphi} + W_{-1}e^{-i\varphi}$  and thus the complex coefficients  $\{K_0, K_{+1}, K_{-1}\}$  from (5) are found by solving the following  $3 \times 3$  linear system:

$$\left\{ \int_0^{2\pi} \mathbf{F}(\phi) d\phi \right\} \cdot \begin{bmatrix} K_0 \\ K_{+1} \\ K_{-1} \end{bmatrix} = \begin{bmatrix} W_0 \\ W_{+1} \\ W_{-1} \end{bmatrix}, \quad (8)$$

where the matrix  $\mathbf{F}(\phi)$  is defined as:

$$\mathbf{F}(\phi) = \begin{bmatrix} F_0(\phi) & F_0(\phi)e^{+i\phi} & F_0(\phi)e^{-i\phi} \\ F_{+1}(\phi) & F_{+1}(\phi)e^{+i\phi} & F_{+1}(\phi)e^{-i\phi} \\ F_{-1}(\phi) & F_{-1}(\phi)e^{+i\phi} & F_{-1}(\phi)e^{-i\phi} \end{bmatrix}.$$

The quantities  $\{W_0, W_{+1}, W_{-1}\}$  and the functions  $\{F_0(\phi), F_{+1}(\phi), F_{-1}(\phi)\}$  are obtained through analytical Fourier integrations and also the integrations in (8) can be carried out rigorously with use of identities as the following:

$$\begin{aligned} \int_0^{2\pi} e^{x \sin \phi + y \cos \phi} d\phi &= 2\pi I_0, \\ \int_0^{2\pi} e^{\pm i\phi + x \sin \phi + y \cos \phi} d\phi &= \pm 2\pi i \frac{x \mp iy}{\sqrt{x^2 + y^2}} I_1, \\ \int_0^{2\pi} e^{\pm 2i\phi + x \sin \phi + y \cos \phi} d\phi &= -2\pi \frac{x \mp iy}{x \pm iy} I_2, \end{aligned} \quad (9)$$

valid for arbitrary complex  $x, y \in \mathbb{C}$ , while  $I_v$  is the  $v$ th order, first-type modified Bessel function evaluated for argument  $\sqrt{x^2 + y^2}$ . It should be noted that the primary part of the Green's function  $G_{\text{prim}}$  can be handled fully analytically with use of its related Fourier expansion [43], while the secondary term  $G_{\text{sec}}$  in (2) gives finally rapidly convergent integrals of  $\beta$ .

## IV. MULTIPLE RODS METASURFACE

### A. Mathematical formulation

A substantially different system response with considerably increased power can be achieved as follows. Instead of a single small cylinder, which generates cylindrical waves, we put an elementary planar metasurface, consisting of infinite periodically distributed identical cylinders, at the same maximal signal position  $z = -g$ . So, let us consider a set of infinite cylindrical PMC rods of radius  $a$  placed on  $(z_m, x_m) = (-g, 2bm)$  with  $m \in \mathbb{Z}$  and  $2b$  the distance between two consecutive rods. Due to the optically small cross section of the rods ( $k_0a \ll 1$ ), constant axial surface magnetic currents  $M_m$  will be induced on them (following similar considerations to those of Sec. III).

The uniform excitation and infinite planar background lead to an equal phase difference  $e^{i2k_0b \sin \theta}$  between the unknown currents of two consecutive cylinders; therefore,  $M_m = M e^{-i2mk_0b \sin \theta}$  describes the current of the  $m$ th cylinder, where  $M$  is the current of the central ( $m = 0$ ) rod. The total scattered field is equal to the infinite sum of scattered fields generated by equivalent bilayer structures where only the  $m$ th cylinder is present at its corresponding position  $(z_m, x_m)$ . In this way, the sole unknown current  $M$  is determined by imposing the boundary condition of the vanishing magnetic field, only once, at  $(z, x) = (-g, 0)$ , where the central rod is situated [46]. This current expression, respective to (3), reads

$$M = \frac{H_{\text{back}}(-g, 0)}{\left(i \frac{k_0}{\eta_0}\right) (2\pi a) \left[-\frac{i}{4} H_0^{(2)}(k_1 a) + S_{\text{prim}} + S_{\text{sec}}\right]}, \quad (10)$$

where

$$S_{\text{prim}} = -\frac{i}{2} \sum_{m=1}^{+\infty} \cos(2mk_0b \sin \theta) H_0^{(2)}(2k_1bm) \quad (11)$$

and

$$S_{\text{sec}} = \frac{\pi}{b} \sum_{n=-\infty}^{+\infty} \left\{ \begin{array}{l} A(u_n, -g) e^{\kappa_1(u_n)g} \\ + B(u_n, -g) e^{-\kappa_1(u_n)g} \end{array} \right\} \quad (12)$$

are the contributions of the primary (except for the  $n = 0$  term) and secondary parts of the Green's function, respectively, while  $u_n = k_0 \sin \theta + n\pi/b$ .

The quantity  $S_{\text{prim}}$ , is evaluated via direct summation, as the medium surrounding the rod is (even slightly) lossy ( $\text{Im}[\varepsilon_1] \neq 0$ ), and hence the involved sums of Hankel functions converge rapidly [47]. Moreover, the infinite sums of  $S_{\text{sec}}$  can be easily proven to converge exponentially. It should be stressed that, in obtaining (12), we employed the well-known Poisson summation formula [48],  $\sum e^{i2bm(\beta - k_0 \sin \theta)} = \frac{\pi}{b} \sum \delta(\beta - u_n)$ , to convert the spectral integrals with respect to  $\beta$  of (2) into series with respect to  $n$  ( $\delta$  is for Dirac delta function). Also, by means of the same formula, we derive the scattered magnetic field into vacuum ( $z < -h_1$ ):

$$\begin{aligned} H_{\text{scat}} &= \left(-i \frac{k_0}{\eta_0}\right) (2\pi a) \frac{\pi}{b} M \\ &\times e^{-ik_0x \sin \theta} \sum_{n=-\infty}^{+\infty} R(u_n, -g) e^{\kappa_0(u_n)z} e^{-in\pi x/b}. \end{aligned} \quad (13)$$

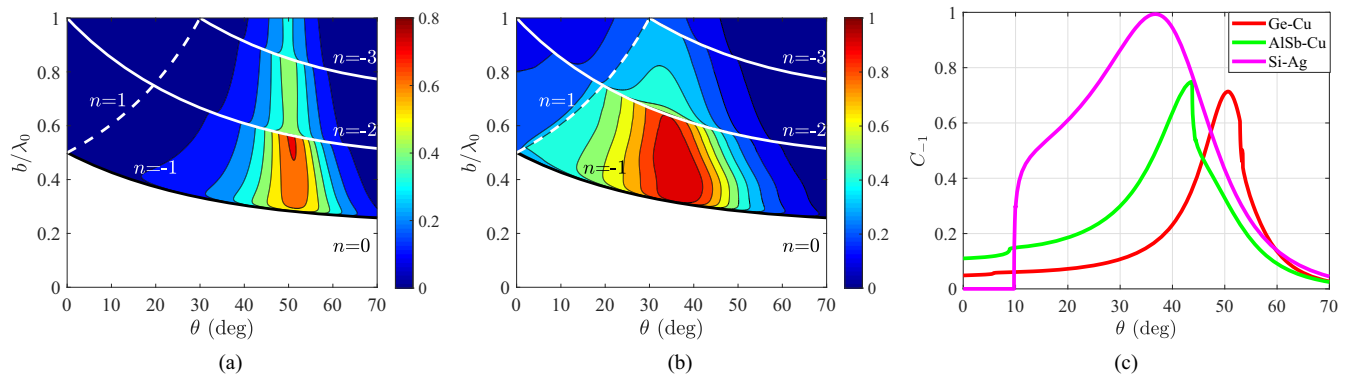


FIG. 6. Variation of the  $C_{-1}$  coefficient on the map of the incidence angle  $\theta$  and the half-distance between two consecutive rods, normalized by the corresponding wavelength  $b/\lambda_0$ , for (a) a Ge-Cu and (b) a Si-Ag bilayer. Black lines divide the plot into regions where only the  $n = 0$  waves are nonevanescant (blank when  $C_{-1}$  is not defined) and regions where other reflective orders are activated. Solid white lines designate the activation of negative reflective orders ( $n > -1$ ), while dashed white lines indicate the activation of positive reflective orders ( $n > 0$ ). (c) Variation of the  $C_{-1}$  coefficient as a function of  $\theta$  for a Ge-Cu, an AlSb-Cu, and a Si-Ag metamirror design.

Likewise  $S_{\text{sec}}$ , the expression of  $H_{\text{scat}}$  converges exponentially, as it comprises terms of the Green's function secondary part. Furthermore, the  $n$ th reflected order of the electromagnetic field is propagating provided that the following conditions are true [27,49]:

$$-\frac{k_0 b}{\pi}(1 + \sin \theta) \leq n \leq \frac{k_0 b}{\pi}(1 - \sin \theta). \quad (14)$$

## B. Numerical results

Since the proposed bilayers exhibit remarkable absorbing capabilities, we investigate below the operation of the multiple-rod structure as a reflective metasurface or metamirror. Explicitly, the direction and power of certain reflected waves can be designed to be controllable and of practical use in relevant applications. The amplitude, direction, and phase of all propagating reflected waves depend on the characteristics of the bilayer configuration, namely the angle of incidence  $\theta$  and the distance  $2b$  between two consecutive rods. Initially, we first analyze the reflection directions of the  $n$ th propagating order, which, by means of (13), is found to be  $\theta_n = \arcsin(\sin \theta + \frac{n\pi}{k_0 b})$ , where the angle  $\theta_n$  is measured clockwise with respect to the  $x$  axis. Observe that, for  $n = 0$ , Eq. (14) is always valid and the zeroth order angle is that dictated by Snell's law. Conversely, plane waves of certain orders  $n < 0$ , for which  $\theta_n \leq 0$ , correspond to reflected contributions towards the same quarter-plane from which the illumination is coming (anomalous diffraction).

To examine the power of those anomalously [50] reflected waves, we introduce the steering power coefficient:

$$C_n = \frac{\delta_{n0} P_{\text{ref}} + P_n}{P_{\text{ref}} + \sum_{m \in \mathcal{P}} P_m}, \quad (15)$$

where  $P_m$  is the power of the  $m$ th reflected order,  $P_{\text{ref}}$  is the reflected power by the bilayer structure (without the rods),  $\mathcal{P}$  denotes the set of all propagating reflected orders, and  $\delta$  is the Kronecker delta. It is stated that only the vertical to the metasurface power components (given by the  $\cos \theta_n / \cos \theta$  ratio) are considered, since they are solely responsible for conveying power away from our setup. Evidently,  $C_n$  would get maximized for certain bilayer setups and reflective orders  $n$  with reflective angles  $\theta_n$ . To this aim, we focus on coefficient  $C_{-1}$  as a function of the period  $2b$  because  $n = -1$  is the first reflective order which corresponds to nonevanescant waves for the smallest possible  $2b$  and every  $\theta$ .

In this framework, Figs 6(a) and 6(b) present the  $C_{-1}$  variation for a Ge-Cu and a Si-Ag metamirror, respectively, versus the half-period to wavelength ratio,  $b/\lambda_0$ , and angle  $\theta$ . Black lines divide the graphs into parts where only  $n = 0$  waves are nonevanescant (blank areas where  $C_{-1}$  not defined) and parts where other reflective orders are activated. Solid white lines designate the activation of negative reflective orders ( $n < -1$ ), while dashed white lines that of positive reflective orders ( $n > 0$ ). It can be deduced that black and white lines intersect only for the  $(\theta = 0^\circ, b = \lambda_0/2)$  pair, as proved via (14); furthermore,  $C_{-1}$  receives substantial values only when

TABLE II. Three bilayer designs from Table I and their respective optimal characteristics (operational frequency  $f$ , angle of incidence  $\theta$ , and half-period  $b$ ) to achieve maximal anomalous reflection  $C_{-1}$  from (15) with simple metasurfaces comprising PMC pins. The frequencies are indicated by the corresponding color of the visible spectrum.

	$f$	$\theta$	$b$	$C_{-1}$	$\theta_{-1}$
Ge-Cu	400 THz	50.66°	417 nm	71.14%	-7.2°
AlSb-Cu	550 THz	43.72°	322 nm	74.81%	-8.9°
Si-Ag	740 THz	36.72°	173 nm	99.37%	-34.8°

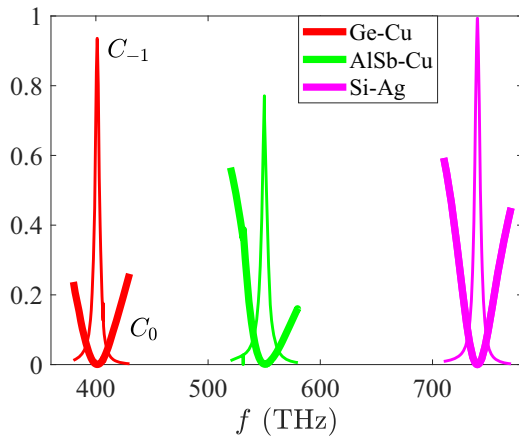


FIG. 7.  $C_0$  coefficients (thick lines) and  $C_{-1}$  coefficients (thin lines) versus the operating frequency  $f$  for three PMC reflective metasurfaces: Ge-Cu (red lines), AlSb-Cu (green lines), and Si-Ag (violet lines). The color of all lines correspond to the color of their operating frequencies.

the  $n = 0$  and  $n = -1$  orders are present and declines notably when other orders are developed. As detected, the maximum  $C_{-1}$  lies very close to the  $n = -2$  line in Fig. 6(a) and almost in the middle of the region between the  $n = -1$  and  $n = -2$  lines in Fig. 6(b). Similar plots, yet with smaller values, can be obtained for the steering power coefficients of other ( $n \neq -1$ ) orders.

Based on our analysis, a plethora of metamirror designs can be proposed in order to achieve high absorption and adjustable reflection at different steering angles, while operating at various angles of incidence  $\theta$  and frequencies  $f$ . Next, we analyze the steering power coefficient  $C_{-1}$ 's dependence on the incident angle  $\theta$  [Fig. 6(c)] and operating frequency (Fig. 7). For this purpose three metasurface designs are examined, all of which work optimally at three distinct angles  $\theta$  and frequencies  $f$ . The characteristics of these metasurfaces are included in Table II (each one working at a different color of the visible light) and are in correspondence with the bilayer's geometrical parameters of Table I. As exhibited in Fig. 6(c), either smaller or larger intervals of angle  $\theta$  can hold high values of the  $C_{-1}$  coefficient, which translates to both wide-angle and narrow-angle performance of our metamirrors around their respective optimal incident angle  $\theta$ . It is worth noting that these optimal angles  $\theta$  and their respective reflecting angles  $\theta_{-1}$  can vary substantially up to  $40^\circ$  among different configurations. That characteristic allows us to pick the appropriate metasurfaces relying upon the direction they are illuminated or the direction we desire our metasurfaces to reflect upon.

Interestingly, the metamirror optimal incidence angle  $\theta$  in Table II may be slightly different from the corresponding bilayer one in Table I. This is due to the fact that  $\theta$  in Table I is selected based on the optimal absorption of visible light and, although high absorption generally implies low reflection levels, the maximum percentage of power reflected toward the  $\theta_{-1}$  direction occurs for similar, yet somewhat different,  $\theta$ . Moreover, since the designs in the prior tables were optimized

via different criteria, there is an anticipated discrepancy between the operational frequencies of Table I and the optimal frequencies of Table II.

This feature is also displayed in Fig. 7, where coefficients  $C_0$  and  $C_{-1}$  are plotted as functions of the operational frequency  $f$  for three PMC metasurfaces. As discerned, high  $C_{-1}$  values can be obtained for frequency ranges of up to 40 THz, which states that it is possible to attain wideband steering of visible illumination at unusual angles. Actually, this is the reason why—despite the fact that some of the metamirror operational frequencies in Figs. 6(a) and 6(c) are not set to their optimal values—the specific designs still attain remarkable  $C_{-1}$  values. Finally, as expected, coefficients  $C_0$  in Fig. 7 decrease significantly, when the  $C_{-1}$  ones become maximum, since  $C_{-1}$  is a part of the  $C_0$  denominator, in (15), and the reflected power from the bilayer structure (without the rods),  $P_{\text{ref}}$ , is meant to diminish in this frequency region.

## V. CONCLUSIONS

An elementary class of wide-angle absorbing bilayers comprising one dielectric and one plasmonic slab is used for wavefront manipulation purposes by exploiting the local field enhancement into the insulating film. Once an impenetrable pin is placed at the maximal signal position, the response of the structure to any incident plane wave is a cylindrical omnidirectional reflection admitting it to work as an efficient small-power wavefront converter. On the other hand, multiple rods, properly placed across the strong-field region, can lead to substantial anomalous diffraction that channels the reflective ray along various directions. Numerous media textures are considered being operated under visible light illumination; every single combination of them is optimized to give highly performing designs. A major weak point of the proposed structures is their substantially lossy background setups which mitigate their overall response. However, they are the simplest possible ones that can guarantee low profile and increased electromagnetic compatibility with other photonic equipment in their spatial vicinity.

These response transformations are proven very instructive in photonic signal processing components, like communication channel ports and nanoreflectarray antennas. Therefore, when combined with the plethora of provided optimal designs, this study may offer increased flexibility in modeling device layouts that control reflectivity, with great practical significance in several wavefront engineering applications. Importantly, the proposed ultrathin metamirror concept can be modified to support arbitrary tailoring of the reflections by suitable selection and spatial distribution of scatterers [51] or by employing cascaded layers [52] of different materials.

## ACKNOWLEDGMENTS

C.V. would like to thank Professor G. Fikioris (National Technical University of Athens, Athens, Greece) for useful discussions on integrals expressed in terms of modified Bessel functions. This work was partially supported by Nazarbayev University Faculty Development Competitive Research Grants No. 021220FD4051 entitled “Optimal Design

of Photonic and Quantum Metamaterials.” The major part of this study was produced in the framework of the visit of A.N.P.

to the School of Sciences and Humanities of Nazarbayev University.

- 
- [1] N. Yu and F. Capasso, Flat optics with designer metasurfaces, *Nat. Mater.* **13**, 139 (2014).
- [2] A. Arbabi, Y. Horie, M. Bagheri, and A. Faraon, Dielectric metasurfaces for complete control of phase and polarization with subwavelength spatial resolution and high transmission, *Nat. Nanotechnol.* **10**, 937 (2015).
- [3] N. M. Estakhri, C. Argyropoulos, and A. Alù, Graded metascreens to enable a new degree of nanoscale light management, *Philos. Trans. A* **373**, 20140351 (2015).
- [4] F. Monticone, N. Estakhri, and A. Alù, Full Control of Nanoscale Optical Transmission with a Composite Metascreen, *Phys. Rev. Lett.* **110**, 203903 (2013).
- [5] C. Pfeiffer and A. Grbic, Metamaterial Huygens’ Surfaces: Tailoring Wave Fronts with Reflectionless Sheets, *Phys. Rev. Lett.* **110**, 197401 (2013).
- [6] K. Achouri, M. Salem, and C. Caloz, General metasurface synthesis based on susceptibility tensors, *IEEE Trans. Antenna Propag.* **63**, 2977 (2015).
- [7] F. Liu, O. Tsilipakos, A. Ptilakis, A. C. Tasolamprou, M. S. Mirmoosa, N. V. Kantartzis, D.-H. Kwon, M. Kafesaki, C. M. Soukoulis, and S. A. Tretyakov, Intelligent Metasurfaces with Continuously Tunable Local Surface Impedance for Multiple Reconfigurable Functions, *Phys. Rev. Applied* **11**, 044024 (2019).
- [8] O. Tsilipakos, A. C. Tasolamprou, T. Koschny, M. Kafesaki, E. N. Economou, and C. M. Soukoulis, Pairing toroidal and magnetic dipole resonances in elliptic dielectric rod metasurfaces for reconfigurable wavefront manipulation in reflection, *Adv. Optical Mater.* **6**, 1800633 (2018).
- [9] A. Minovich, A. Miroshnichenko, A. Bykov, T. Murzina, D. Neshev, and Y. Kivshar, Functional and nonlinear optical metasurfaces, *Laser Photon. Rev.* **9**, 195 (2015).
- [10] N. Shitrit, J. Kim, D. Barth, H. Ramezani, Y. Wang, and X. Zhang, Asymmetric Free-Space Light Transport at Nonlinear Metasurfaces, *Phys. Rev. Lett.* **121**, 046101 (2018).
- [11] D. Pozar, S. Targonski, and H. Syrigos, Design of millimeter wave microstrip reflectarrays, *IEEE Trans. Antenna Propag.* **45**, 287 (1997).
- [12] A. Díaz-Rubio, J. Li, C. Shen, S. Cummer, and S. Tretyakov, Power flow-conformal metamirrors for engineering wave reflections, *Sci. Adv.* **5**, eaau7288 (2019).
- [13] A. Arbabi, E. Arbabi, Y. Horie, S. Kamali, and A. Faraon, Planar metasurface retroreflector, *Nat. Photon.* **11**, 415 (2017).
- [14] V. Asadchy, Y. Ra’di, J. Vehmas, and S. Tretyakov, Functional Metamirrors Using Bianisotropic Elements, *Phys. Rev. Lett.* **114**, 095503 (2015).
- [15] H. Wakatsuchi, S. Kim, J. Rushton, and D. Sievenpiper, Waveform-Dependent Absorbing Metasurfaces, *Phys. Rev. Lett.* **111**, 245501 (2013).
- [16] B. Ratni, A. Lustrac, G.-P. Piau, and S. Burokur, Reconfigurable meta-mirror for wavefronts control: applications to microwave antennas, *Opt. Express* **26**, 2613 (2018).
- [17] M. Pu, P. Chen, Y. Wang, Z. Zhao, C. Huang, C. Wang, X. Ma, and X. Luo, Anisotropic meta-mirror for achromatic electromagnetic polarization manipulation, *Appl. Phys. Lett.* **102**, 131906 (2013).
- [18] A. Papadimopoulos, N. Kantartzis, N. Tsitsas, and C. Valagiannopoulos, Wide-angle absorption of visible light from simple bilayers, *Appl. Opt.* **56**, 9779 (2017).
- [19] M. Gjerding, R. Petersen, T. Pedersen, N. Mortensen, and K. Thygesen, Layered van der Waals crystals with hyperbolic light dispersion, *Nat. Commun.* **8**, 1 (2017).
- [20] L. Ranno, S. Dal Forno, and J. Lischner, Computational design of bimetallic core-shell nanoparticles for hot-carrier photocatalysis, *Npj Comput. Mater.* **4**, 1 (2018).
- [21] E. Shapera and A. Schleife, Database-driven materials selection for semiconductor heterojunction design, *Adv. Theor. Simul.* **1**, 1800075 (2018).
- [22] C. Valagiannopoulos, Photonic inverse design of simple particles with realistic losses in the visible frequency range, *Photonics* **6**, 23 (2019).
- [23] R. Li, Z. Guo, W. Wang, J. Zhang, K. Zhou, J. Liu, S. Qu, S. Liu, and J. Gao, Arbitrary focusing lens by holographic metasurface, *Photon. Res.* **3**, 5 (2015).
- [24] Q. Sun, Z. Zhang, Y. Huang, X. Ma, M. Pu, Y. Guo, X. Li, and X. Luo, Asymmetric transmission and wavefront manipulation toward dual-frequency meta-holograms, *ACS Photonics* **6**, 1541 (2019).
- [25] V. Popov, S. N. Burokur, and F. Boust, Conformal Sparse Metasurfaces for Wavefront Manipulation, *Phys. Rev. Appl.* **14**, 044007 (2020).
- [26] V. Asadchy, A. Diaz-Rubio, S. Tsvetkova, D.-H. Kwon, A. Elsakka, M. Albooyeh, and S. Tretyakov, Flat Engineered Multichannel Reflectors, *Phys. Rev. X* **7**, 031046 (2017).
- [27] N. Tsitsas and C. A. Valagiannopoulos, Anomalous reflection of visible light by all-dielectric gradient metasurfaces, *J. Opt. Soc. Am. B* **34**, D1 (2017).
- [28] A. Wong and G. Eleftheriades, Perfect Anomalous Reflection with a Bipartite Huygens Metasurface, *Phys. Rev. X* **8**, 011036 (2018).
- [29] S. Kim, H. Wakatsuchi, J. Rushton, and D. Sievenpiper, Switchable nonlinear metasurfaces for absorbing high power surface waves, *Appl. Phys. Lett.* **108**, 041903 (2016).
- [30] S. Kruk, F. Ferreira, N. Mac Suibhne, C. Tsekrekos, I. Kravchenko, A. Ellis, D. Neshev, S. Turitsyn, and Y. Kivshar, Transparent dielectric metasurfaces for spatial mode multiplexing, *Laser Photon. Rev.* **12**, 8 (2018).
- [31] C. Valagiannopoulos, T. Tsiftsis, and V. Kovanis, Metasurface-enabled interference mitigation in visible light communication architectures, *J. Opt.* **21**, 115702 (2019).
- [32] J. Zhang, Y. Li, X. Zhang, and B. Yang, Colloidal self-assembly meets nanofabrication: From two-dimensional colloidal crystals to nanostructure arrays, *Adv. Mater.* **22**, 4249 (2010).

- [33] Z. Huang, H. Fang, and J. Zhu, Fabrication of silicon nanowire arrays with controlled diameter, length, and density, *Adv. Mater.* **19**, 744 (2007).
- [34] R. Hobbs, N. Petkov, and J. Holmes, Semiconductor nanowire fabrication by bottom-up and top-down paradigms, *Chem. Mater.* **24**, 1975 (2012).
- [35] K. W. Schwarz and J. Tersoff, From Droplets to Nanowires: Dynamics of Vapor-Liquid-Solid Growth, *Phys. Rev. Lett.* **102**, 206101 (2009).
- [36] C.-T. Tai, *Electromagnetic Theory of Gratings*, first ed. (Intext Educational Publishers, University of Michigan, 1971).
- [37] C. A. Balanis, *Advanced Engineering Electromagnetics*, second ed. (John Wiley & Sons, Inc., New York, 2012).
- [38] F. Gömöry, M. Solovyov, J. Šouc, C. Navau, J. Prat-Camps, and A. Sanchez, Experimental realization of a magnetic cloak, *Science* **335**, 1466 (2012).
- [39] R. Sharif, S. Shamaila, M. Ma, L. D. Yao, R. C. Yu, X. F. Han, and M. Khaleeq-ur-Rahman, Magnetic switching of ferromagnetic nanotubes, *Appl. Phys. Lett.* **92**, 032505 (2008).
- [40] H. Ohno, Making nonmagnetic semiconductors ferromagnetic, *Science* **281**, 951 (1998).
- [41] C. A. Valagiannopoulos, A. Tukiainen, T. Aho, T. Niemi, M. Guina, S. A. Tretyakov, and C. R. Simovski, Perfect magnetic mirror and simple perfect absorber in the visible spectrum, *Phys. Rev. B* **91**, 115305 (2015).
- [42] C. Valagiannopoulos, Closed-form solution to the scattering of a skew strip field by metallic pin in a slab, *Prog. Electromagn. Res.* **79**, 1 (2008).
- [43] C. Valagiannopoulos, Study of an electrically anisotropic cylinder excited magnetically by a straight strip line, *Prog. Electromagn. Res.* **73**, 297 (2007).
- [44] C. Valagiannopoulos, A novel methodology for estimating the permittivity of a specimen rod at low radio frequencies, *J. Electromagn. Waves Appl.* **24**, 631 (2010).
- [45] P. A. Martin, *Multiple Scattering, Interaction of Time-Harmonic Waves with  $N$  Obstacles* (Cambridge University Press, Cambridge, UK, 2006).
- [46] I. Liberal, I. S. Nefedov, I. Ederra, R. Gonzalo, and S. A. Tretyakov, Electromagnetic response and homogenization of grids of ferromagnetic microwires, *J. Appl. Phys.* **110**, 064909 (2011).
- [47] I. Liberal, I. S. Nefedov, I. Ederra, R. Gonzalo, and S. A. Tretyakov, On the effective permittivity of arrays of ferromagnetic wires, *J. Appl. Phys.* **110**, 104902 (2011).
- [48] P. Morse and H. Feshbach, *Methods of Theoretical Physics*, Part I (McGraw-Hill Book Company Inc., New York, 1953).
- [49] Z. Tagay and C. Valagiannopoulos, Highly selective transmission and absorption from metasurfaces of periodically corrugated cylindrical particles, *Phys. Rev. B* **98**, 115306 (2018).
- [50] H. Wallén, H. Kettunen, and A. Sihvola, Anomalous absorption, plasmonic resonances, and invisibility of radially anisotropic spheres, *Radio Sci.* **50**, 18 (2015).
- [51] T. Rimpilainen, H. Wallén, and A. Sihvola, Radial anisotropy in spheroidal scatterers, *IEEE Trans. Antennas Propag.* **63**, 3127 (2015).
- [52] A. Sarsen and C. Valagiannopoulos, Robust polarization twist by pairs of multilayers with tilted optical axes, *Phys. Rev. B* **99**, 115304 (2019).